nature communications

Article

https://doi.org/10.1038/s41467-024-54278-y

A high-response-frequency bimodal network polyacrylate elastomer with ultrahigh power density under low electric field

Received: 5 May 2024

Accepted: 6 November 2024

Published online: 13 November 2024

Check for updates

Li-Juan Yin[1], Boyuan Du[2], Hui-Yi Hu[1], Wen-Zhuo Dong[1], Yu Zhao[3], Zili Zhang[3], Huichan Zhao[2], Shao-Long Zhong[1,4], Chenyi Yi[1], Liangti Qu[5] & Zhi-Min Dang[1]

Dielectric elastomers, used as driver modules, require high power density to enable fast movement and efficient work of soft robots. Polyacrylate elastomers usually suffer from low power density under low electric fields due to limited response frequency. Here, we propose a bimodal network polyacrylate dielectric elastomer which breaks the intrinsic coupling relationship between dielectric and mechanical properties, featuring relatively high dielectric constant, low Young's modulus, and wide driving frequency bandwidth (~200 Hz) like silicones. Therefore, an ultrahigh power density (154 W kg^{-1}@20 MV m^{-1}, 200 Hz) is realized at low electric field and high resonance frequency, 75 times greater than at 10 Hz. Further, a rotary motor is developed, reaching an impressive speed of 1245 rpm at 19.6 MV m^{-1} and 125 Hz, surpassing previous acrylate-based motors and entering the high-speed domain of silicone-based motors. These findings offer a versatile strategy to fabricate high-power-density dielectric elastomers for low-electric-field soft actuators.

Dielectric elastomers (DEs), a class of electroactive polymers, are renowned for their substantial reversible deformation under electric fields, directly converting electrical energy into mechanical energy. They exhibit significant advantages, including large deformation (>100%), high energy density (up to 3.4 MJ m^{-3}), high energy conversion efficiency (over 80% theoretically)[1–3]. Due to the intrinsic characteristics of high compliance, light weight and low noise[4–7], dielectric elastomer actuators (abbreviated as DEAs) have drawn widespread attention in various fields of soft robotics[8] and biomedical applications[9,10], such as aerial robots with controllable flight[4,11,12], climbing robots[10,13], deep-sea biomimetic snailfish[14], soft non-magnetic motors[15–18], versatile grippers[19,20], and electrically tunable silicone lenses[21]. As the driving and power modules for soft actuators, the power density of dielectric elastomers is pivotal for enabling DEAs to perform complex movements like crawling, flying, and swimming, as well as to output work[4,22]. Enhancing the power density not only augments the propulsion capabilities but also broadens the horizons for the advancement of soft actuators, particularly within the realm of microminiature systems[4,11,12]. For example, Chen et al[4] theoretically and experimentally demonstrated that only when the power density of a flapping wing microrobot reaches 200 W kg^{-1} can it overcome its weight and take off. Up till now, the power density of numerous previously-reported dielectric elastomers has reached even exceeded that of natural human muscles (typical value: 50 W kg^{-1}, maximum value: 284 W kg^{-1})[23], which roundly facilitates the development of dielectric elastomer actuators, demonstrating great potential in the fields of soft robotics.

Currently, compared with that on the electrically-driving strain, the research on the power density of dielectric elastomers is comparatively scarce and predominantly concentrated on acrylic elastomers[3,24,25] and silicones[4,11,22]. Power density is determined by the product of energy density and driving frequency. The energy density,

[1]State Key Laboratory of Power System Operation and Control, Department of Electrical Engineering, Tsinghua University, Beijing, China. [2]Department of Mechanical Engineering, Tsinghua University, Beijing, China. [3]School of Electrical Engineering, Zhengzhou University, Zhengzhou, China. [4]State Key Laboratory of Electrical Insulation and Power Equipment, Xi'an Jiaotong University, Xi'an, China. [5]Department of Chemistry, Tsinghua University, Beijing, China. e-mail: dangzm@tsinghua.edu.cn

in turn, is nearly proportional to the square of the dielectric constant, inversely related to Young's modulus, and directly proportional to the fourth power of the driving electric field amplitude (for detailed illustration, please refer to "Calculation of power density under different driving frequencies" in the Supplementary Discussion). Consequently, the power density of dielectric elastomers is dependent on a combination of the polymers' intrinsic dielectric and mechanical properties, as well as the intensity of the applied driving electric fields.

Acrylic elastomers have satisfactory energy density[2] but low response frequency[26] due to severe viscoelasticity. Duduta et al.[25] prepared various multilayer dielectric elastomers via three acrylic oligomers and then obtained the power density of 2.04 W kg^{-1}, 19.5 W kg^{-1}, 42.6 W kg^{-1} at the driving field of 100 MV m^{-1} and driving frequencies of 1 Hz, 10 Hz, 30 Hz, respectively. Subsequently, they fabricated multilayer actuators using the above DEs and carbon nanotubes as compliant electrodes and achieved higher power densities of 30 ~ 80 W kg^{-1} under electric fields of 100 ~ 150 MV m^{-1} and 1 ~ 10 Hz[24]. Pei et al.[3] synthesized a high-performance acrylic dielectric elastomer with a bimodal network structure which exhibited a power density of ~670 W kg^{-1} under 2.5 kV (>62.5 MV m^{-1}) and 5 Hz with a 1.2 N preload (~0.5 MPa) without additional pre-stretching. For acrylic dielectric elastomers, achieving high power density (>100 W kg^{-1}) usually requires high electric fields due to limited response frequency bandwidth (usually <10 Hz) originating from inherent serious viscoelasticity.

Conversely, silicone elastomers have earned greater interests from researchers due to notably higher response frequency (>100 Hz)[4,12,26]. Zhao et al.[22] fabricated a rolled cylindrical dielectric elastomer actuator using multilayer silicone films and reported a power density of 55 W kg^{-1} at the driving electric field of 40 MV m^{-1} and 200 Hz. Later, they collaborated with Chen et al.[4] and increased the resonance frequency to 500 Hz, achieving an impressive power density of 600 W kg^{-1} @43 MV m^{-1}. The remarkable power density achieved by the rolled dielectric elastomer actuator has enabled the development of flapping-wing aerial robots, facilitating controlled flight. In 2021, Chen et al.[11] increased the power density of rolled actuators to 1200 W kg^{-1} @66 MV m^{-1} and 475 Hz, which is the highest power density reported for silicone elastomers currently. They further incorporated this soft actuator into an aerial robot and obtained a considerable lift-to-weight ratio (>2.2:1), enabling an ascending speed of 70 cm s^{-1}. Subsequently, by refining the spin coating and vacuum filtration process, they presented high-quality 10 μm thin elastomer films which were stacked into a low-voltage (~500 V), long-endurance, and power-dense (>500 W kg^{-1}) DEA via a multiple-layering fabrication method[12]. Reducing the driving electric fields is the fundamental way to lower the overall voltage level of DEAs

Achieving high power density, specifically greater than 100 W kg^{-1}, typically necessitates the application of high driving electric fields. Acrylate polymers, while boasting a high dielectric constant of over 4 at 1 kHz[17], are limited by a narrow bandwidth of less than 10 Hz[3,26–28]. Conversely, silicones offer a more favorable bandwidth exceeding 100 Hz[18,21,29] but possess a relatively lower dielectric constant of approximately 2.8 at 1 kHz[21,30]. However, the use of high electric fields not only complicates the design and operation of driving and control modules but also poses significant safety risks to both devices and humans. Therefore, attaining high power density at lower driving electric fields remains a critical yet challenging objective for the advancement of DEAs.

Here, a high-response-frequency, high-power-density bimodal polyacrylate dielectric elastomer is crosslinked by two crosslinking agents with different molecular chain lengths. Compared with the uniform network crosslinked by macromolecular crosslinking agent, this bimodal network demonstrates suppressed viscoelasticity due to shortened average molecular weight between crosslinking points and constrained molecular chain mobility, giving rise to reduced mechanical loss and elevated response frequency. As a result, the well-designed network not only retains the high dielectric constant (ε_r = 4.35@1 kHz) of the acrylate dielectric elastomers, but also features the low mechanical loss (tan δ_m = 0.125@1 Hz) and high response frequency (~200 Hz) like silicone elastomers, then demonstrating high power density (154 W kg^{-1} @20 MV m^{-1}, 200 Hz) under a low electric field, about 75 times higher than that at 20 MV m^{-1} and 10 Hz. Finally, a DEA rotary motor based on LA-CP-3 has been fabricated, achieving a maximum rotational speed of 1245 rpm under a significantly reduced electric field (19.6 MV m^{-1} at 125 Hz), which is considerably higher than that of previously reported acrylate-based motors (typically below 200 rpm), and now enters the exclusive high-speed domain of silicone-based motors (over 1000 rpm).

Results and discussion

Crosslinked network design and microstructure characteristic

The preparation process and synthesis chemistry of bimodal elastomer network are demonstrated in Fig. 1a, b. The nomenclature of samples was based on the composition and dose of chemicals, where LA stood for reactive monomer (Lauryl Acrylate, LA), C for the macromolecular crosslinking agent (CN9021NS) while P for the small-molecular crosslinking agent (PEGDA), and these figures for the content of PEGDA. The PEGDA content of LA-CP-1, LA-CP-2, and LA-CP-3 is 0.2 wt%, 0.4 wt%, and 0.6 wt%, respectively.

After introducing a slim amount of small-molecular crosslinking agent (PEGDA), the network structure will change, which is illustrated clearly via thorough characterizations. As the concentration of the small-molecular crosslinking agent (PEGDA) increases, there is a corresponding decrease in the swelling ratio of the elastomers, accompanied by an increase in the gel fraction, as depicted in Fig. 1c. This trend suggests that the small-molecular crosslinking agent participates in the formation of the crosslinking network, thereby elevating the crosslinking density of the elastomers. Further, thermal and phase analysis were preformed to investigate the effect of small-molecular crosslinking agent and microstructure of crosslinking networks. The baseline shifts of DSC curves near −60 °C result from the glass transition of macromolecular crosslinking agent and the endothermic peaks near 0 °C are the melting peaks of poly(lauryl acrylate) segments (pLA) (Supplementary Fig. 1). There is almost no difference between the DSC curve of LA-C and LA-CP-3, especially at the temperature above 20 °C. This implies that the small-molecular crosslinking agent does not alter the microstructure or phase composition except increase the chemical crosslinking density. According to DSC and XRD results, there is no crystallization in polymer networks (Fig. 1d and Supplementary Fig. 2), yet there are nanodomains consisting of regular structures (Fig. 1e and Supplementary Fig. 3). Specifically, there are three scattering intensity peaks at ~1 nm^{-1}, ~3 nm^{-1} and ~14 nm^{-1}, respectively. The first scattering peaks near 1 nm^{-1} are due to the testing instrument, which is confirmed by characterizing within a smaller angular range (Supplementary Fig. 4). According to the equation ($q = 4\pi \sin\theta/\lambda$, where q is scattering vector, θ is scattering angle and λ is X-ray wavelength), the maximum scattering dispersion peaks located at ~14 nm^{-1} stem from the amorphous structure whose corresponding diffraction peak is located at $2\theta \sim 20°$ in the XRD spectrum (Supplementary Fig. 2). Most noteworthy, the distinct scattering peaks near 3 nm^{-1} declare the existence of nanodomains (Supplementary Fig. 5) whose size is around 2.2 nm (calculated by $d = 2\pi/q$ where d is the average size of nanodomains)[31]. These nanodomains probably originate from relatively regularly arranged alkyl side chains of reactive monomers (LA)[32–34] (Supplementary Fig. 6), and can act as physical crosslinking points[35]. After normalizing the intensity curves based on their amorphous structure scattering peaks, the peak profiles on WAXS curves are almost identical among different samples (Supplementary Fig. 7). Consequently, the addition of a small-molecular crosslinking agent does not impact

https://doi.org/10.1038/s41467-024-54278-y

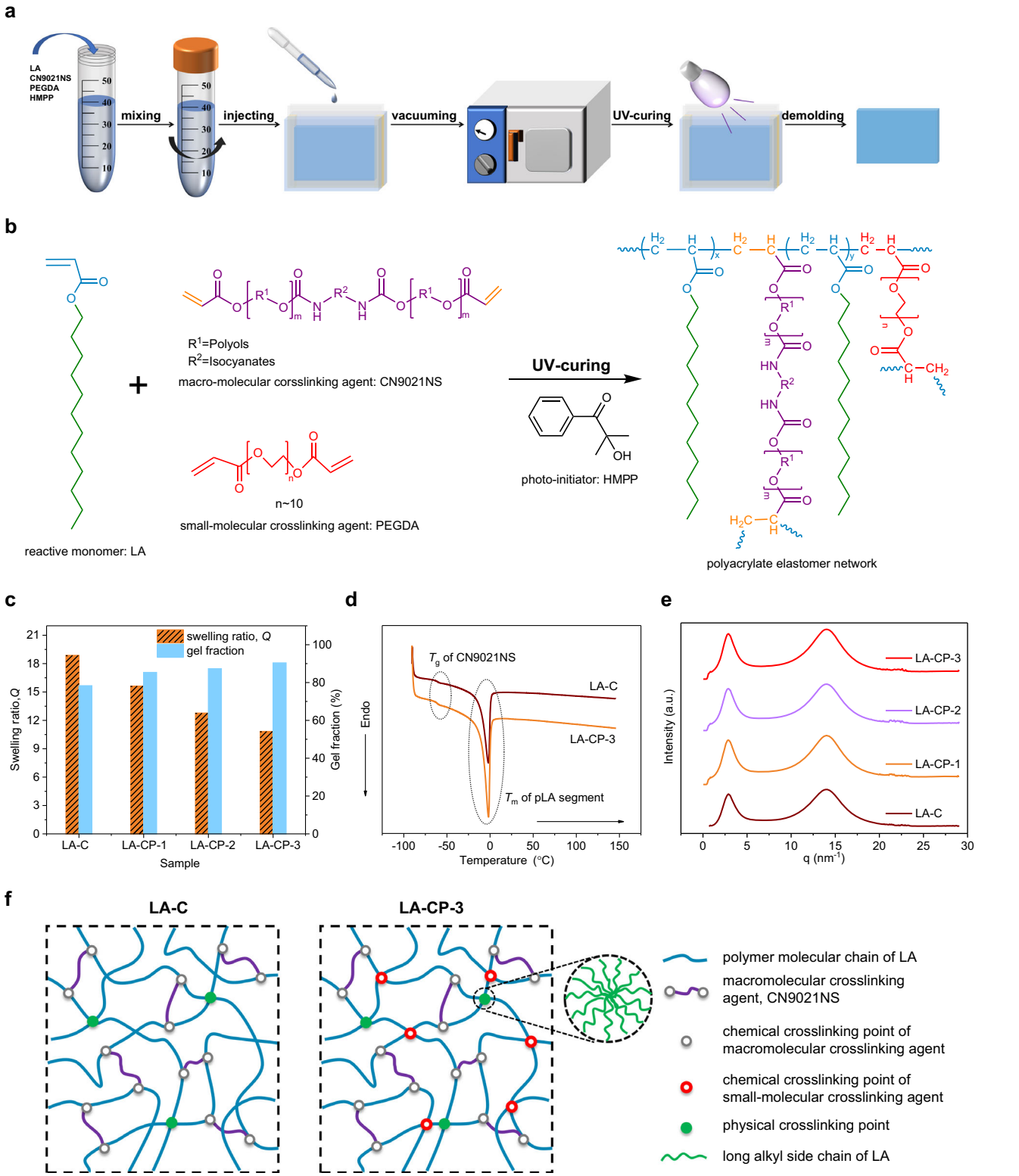

Fig. 1 | Preparation and characterization of elastomer network structure. **a** Diagrammatic drawing of elastomer preparation process. **b** Network synthesis chemistry. **c** Comparison of swelling ratio and gel fraction among different samples. The nomenclature of samples was based on the composition and dose of chemicals, where LA stood for reactive monomer (Lauryl Acrylate, LA), C for the macromolecular crosslinking agent (CN9021NS) while P for the small-molecular crosslinking agent (PEGDA), and these figures for the content of PEGDA. The PEGDA content of LA-CP-1, LA-CP-2, and LA-CP-3 is 0.2 wt%, 0.4 wt%, and 0.6 wt%, respectively. **d** Differential scanning calorimetry (DSC) curves of LA-C and LA-CP-3. The dashed markers in Fig. 1d indicate the glass transition temperature (T_g) of the macromolecular crosslinking agent and the melting temperature (T_m) of poly(lauryl acrylate) segments (pLA). **e** WAXS spectrum of LA-C, LA-CP-1, LA-CP-2, and LA-CP-3. **f** Schematic diagram of the bimodal network with high power density.

https://doi.org/10.1038/s41467-024-54278-y

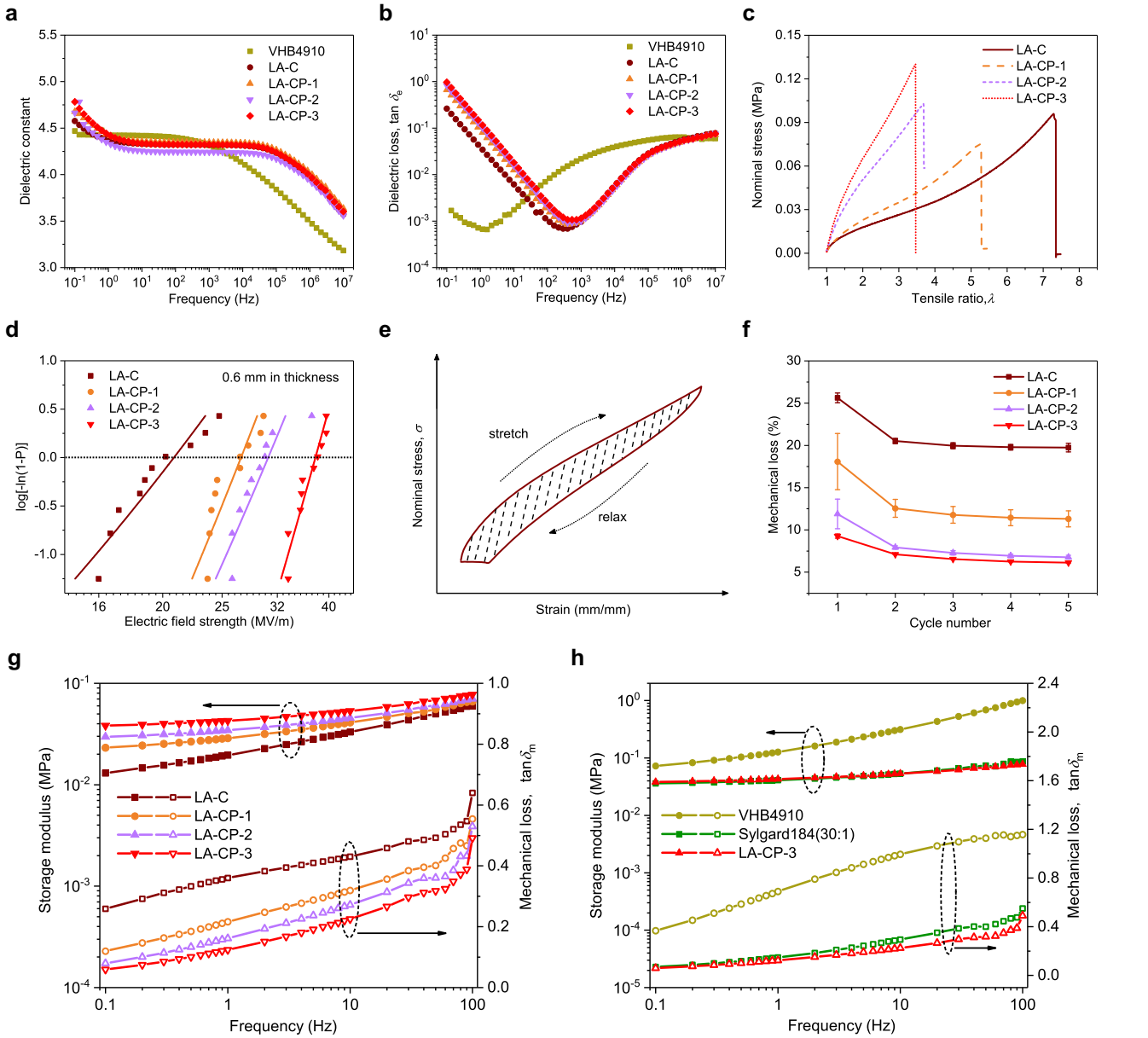

Fig. 2 | Electromechanical properties. a Frequency dependence of dielectric constant and (**b**) dielectric loss (tan δ_e) between commercial acrylic elastomer VHB4910 and our materials. **c** Curves of nominal stress vs tensile ratio. **d** Comparison of electric breakdown strength among the elastomers synthesized in this work. **e** Diagram of the cyclic stress-strain curve. The shaded area enclosed by the stress-strain curve indicates the mechanical loss during one tensile period. **f** Mechanical loss of elastomers. **g** Storage modulus and the tangent of mechanical loss angle (tan δ_m) as a function of frequency of our materials. **h** Frequency-dependent behavior of storage modulus and the tangent of mechanical loss angle (tan δ_m) of commercial elastomers (VHB4910 and Sylgrad 184) and LA-CP-3 designed in this work.

the intrinsic phase structure of the polymer network, specifically the dimensions and quantity of nanodomains.

The above analysis illustrates that there exist nanodomains of ~2.2 nm in network acting as physical crosslinking points and a slight amount of small-molecular crosslinking agent only increases chemical crosslinking density to a certain extent (for detailed information, please refer to "Calculation of crosslink density" in the Supplementary Discussion). Then, the diagrammatic drawing of the networks before and after adding small-molecular crosslinking agent is shown in Fig. 1f. In LA-CP-3, for example, a bimodal network is built using two crosslinking agents with different chain lengths (the number average molecular weight of CN9021NS is 2.8 $\times 10^4$ g mol^{-1} [17] while that of PEGDA is ~516 g mol^{-1}). The use of macromolecular crosslinking agents, characterized by their long, soft, and extended chains, ensures a high degree of elongation for the polymer network. In contrast, the addition of small-molecular crosslinking agents reduces the chain lengths between crosslinking points, thereby stiffening the network. This dual approach allows for the fine-tuning of the stress-strain behavior and viscoelastic properties of the material.

Electromechanical properties

Our materials present relatively high dielectric constant due to ester groups and amino ester groups in the polymer networks (Fig. 2a) but much suppressed dielectric loss and conductivity in the range of 10^2 Hz ~10^4 Hz due to the high flexibility of chain segments and absence of strongly polar groups (Fig. 2b and Supplementary Fig. 8). High dielectric constant signifies more electromechanical coupling energy and low dielectric loss denotes less loss during energy conversion. Introducing

Table 1 | Electromechanical performance comparison of elastomers designed in this work and commercial materials

sample	ε_r@ 1 kHz	tan δ_e@1 kHz	storage modulus (MPa) @1 Hz, 25 °C	tan δ_m @1 Hz, 25 °C	mechanical loss at 5th cycle (%)	frequency bandwidth (Hz)
LA-C	4.32	9.72*10^{-4}	0.020	0.360	19.7	~3
LA-CP-1	4.35	1.02*10^{-3}	0.029	0.216	11.3	~100
LA-CP-2	4.24	9.98*10^{-4}	0.034	0.162	6.77	~200
LA-CP-3	4.32	1.15*10^{-3}	0.043	0.124	6.12	~200
VHB4910	4.32	0.022	0.127	0.690	36.99	~3
Sylgard 184(30:1)[a]	2.99	2.71*10^{-3}	0.041	0.148	5.71	<200

[a]The dielectric properties of Sylgard 184(30:1) is illustrated in Supplementary Fig. 10.

small-molecular crosslinking agent would adjust the stress-strain relationship (Fig. 2c). With the increase in the concentration of PEGDA, strain hardening appears at smaller tensile ratios, which can suppress electromechanical instability (EMI)[3,5,36–38]. Owing to higher Young's modulus and much-suppressed EMI, the LA-CP-3 without pre-stretched demonstrates remarkably improved electric breakdown strengths (LA-C: 20.8 MV m^{-1}; LA-CP-3: 37.5 MV m^{-1}) (Fig. 2d).

Thanks to the bimodal network structure, the viscoelasticity is also significantly modified. As a reference, two widely-used commercial elastomers -VHB4910 (acrylate) and Dowcorning Sylgard 184(30:1) (silicone)-were also measured. Specially, the crosslinker ratio (30:1) of Sylgard 184 is elaborately designed to tune its Young's modulus similar to that of the LA-CP-3. The stress-strain curve under cyclic stretch is illustrated in Fig. 2e, and the encircled area represents the mechanical loss during one stretch period. Therefore, mechanical loss (%) is defined as the ratio of the mechanical energy dissipated during the whole cyclic stretch to the mechanical energy consumed during the unidirectional stretch (for detailed information, please refer to "Calculation of mechanical loss during cyclic stretch" in the Supplementary Discussion). Stress-strain curves of elastomers including their commercial counterparts under uniaxial cyclic stretch present an evident Mullins effect and become thinner with the increase of cycle times (Supplementary Fig. 9). Therefore, the mechanical loss decays as the cycle number rise and saturates after 4 times. With 0.6 wt% PEGDA, the mechanical loss of elastomers reduces by 69%, decreasing from 19.74% (LA-C) to 6.12% (LA-CP-3) (Fig. 2f). And for reference, the mechanical loss of VHB4910 and Sylgard 184(30:1) is 36.99% and 5.71%, respectively. Further, dynamic mechanical analysis (DMA) results also demonstrate that by adding small-molecular crosslinking agent, the mechanical loss (tan δ_m) can remarkably decrease from 0.360@1 Hz (LA-C) to 0.124@1 Hz (LA-CP-3), greatly suppressing the viscoelastic behavior (Fig. 2g). Additionally, the mechanical loss (tan δ_m) of LA-CP-3 is not only much lower than that of the same-category acrylic VHB4910 (0.690@1 Hz) but even slightly lower than that of their silicone counterpart Sylgard184(30:1) (0.148@1 Hz) which has inherent features of low viscoelasticity and low mechanical loss (Fig. 2h). After adding small-molecular crosslinking agent, the desirable dynamic mechanical response can be attributed to the shortened chain lengths between crosslinking points and restrained long-range motion of segments during tension.

Thus, as polyacrylate, the LA-CP-3 has satisfactory mechanical properties even exceeding silicones, and reserves a high dielectric constant at the same time. These satisfactory electromechanical properties indicate high actuation performance. The dielectric and mechanical properties of elastomers synthesized in this work as well as commercial materials are summarized in Table 1.

Electrical actuation properties

Dependence of actuation area strain on nominal driving electric field is shown in Fig. 3a. The maximum area strain of LA-C is 24.62% @10 MV m^{-1} due to premature failure caused by EMI. However, adding small-molecular crosslinking agent, on the one hand, can shift the strain hardening to a lower stretch ratio and suppress EMI, thereby achieving larger area strain at higher driving electric fields. For LA-CP-1, the area strain is 21.60%@13 MV m^{-1}. On the other hand, adding small-molecular crosslinking agent toughs the polymer network and reduces actuation sensitivity (the ratio of dielectric constant to Young's modulus), consequently limiting area strain. The area strain of LA-CP-2 and LA-CP-3 reaches to 16.62%@15 MV m^{-1} and 12.68@15 MV m^{-1}, respectively. Considering the safety of humans and test equipment, the maximum driving electric field is restricted to 15 MV m^{-1}, at which failure does not occur for LA-CP-2 and LA-CP-3. Owing to lower Young's modulus compared to VHB4910 and higher dielectric constant compared to Sylgard 184(30:1), the LA-CP-3 presents noticeably larger area strains than its commercial counterparts (e.g., VHB4910: 2.88%@15 MV m^{-1}; Sylgard 184(30:1): 6.63% @15 MV m^{-1}) (Fig. 3b).

Introducing small-molecular crosslinking agent improves the crosslinking density of the network and shortens the chain lengths between crosslinking points. Accordingly, the propagation speed of stress through the crosslinking network is elevated due to improving material stiffness. The utilization of a small-molecular crosslinking agent has significantly enhanced the performance of our material, as evidenced by frequency response (Fig. 3c, d). *Z*-axis displacements at different frequencies are normalized based on that at 1 Hz, which is denominated as normalized *z*-axis displacement (Fig. 3c, d). And cut-off frequency, which is defined as the frequency at which the displacement amplitude drops to 0.707 of that at 1 Hz[22], is discussed to describe the displacement response bandwidth. As the content of small-molecular crosslinking agent rises, the frequency response of elastomers is promoted clearly due principally to elevated moduli and limited viscoelastic loss. The displacement frequency response for LA-C shows a straight decline within 100 Hz. Nevertheless, the LA-CP-3 with 0.6 wt% PEGDA exhibits a broad, almost frequency-independent response up to ~100 Hz, followed by amplitude increase, and then the response rolls off sharply. Consequently, the LA-CP-3 also exhibits about two orders of magnitude higher bandwidth than LA-C, rising from less than 3 Hz to ~200 Hz. Notably, each sample displays two discernable resonant frequencies which depend on elastomer and electrode combination as well as structural dimension. Generally, high modulus and low tan δ_m facilitate to achieve broad bandwidth. Due to high viscoelasticity (tan δ_m = 0.690 @1 Hz), VHB4910, as a typical polyacrylate, exhibits severe damping and loses resonance peak, which results in low bandwidth (<3 Hz) even with a stiffer network (Fig. 3d). Thus, with similar mechanical properties to LA-CP-3, Sylgard 184(30:1), a typical silicone elastomer, exhibits comparable frequency response performance with LA-CP-3 within 200 Hz. Typically, polyacrylates feature unsatisfactory frequency response characteristics in contrast with silicones due to serious viscoelasticity. Here, with only 0.6 wt% PEGDA, LA-CP-3, an acrylic dielectric

https://doi.org/10.1038/s41467-024-54278-y

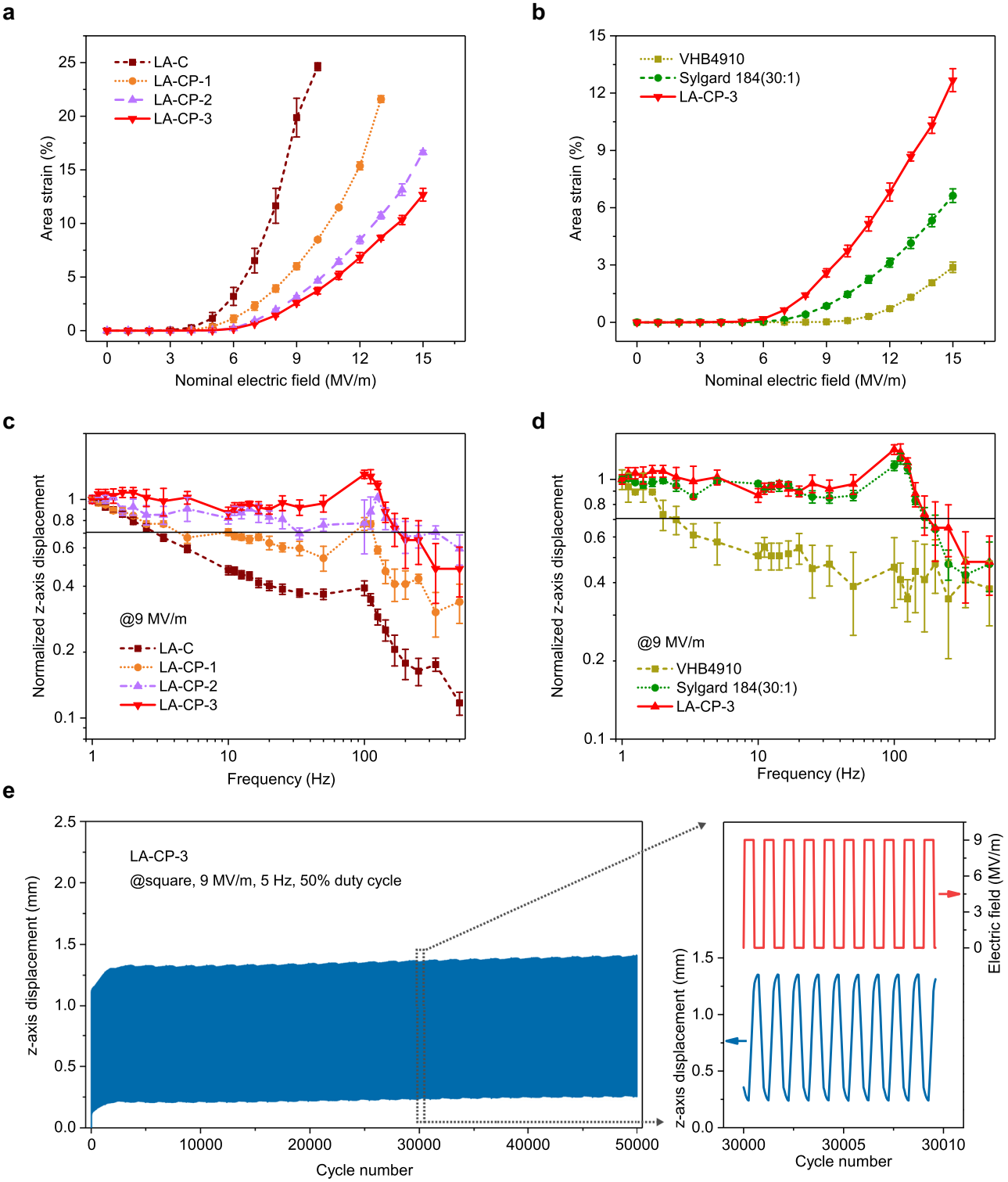

Fig. 3 | Electrical actuation performance. a Dependence of actuated area strain on the nominal driving electric field for LA-C, LA-CP-1, LA-CP-2, and LA-CP-3. **b** Dependence of actuated area strain on the nominal driving electric field for commercial elastomers (VHB4910 and Sylgard 184) and LA-CP-3. **c** Frequency response of samples under 9 MV m^{-1} in the range of 1 Hz–500 Hz. The *z*-axis displacement was normalized to 1 at 1 Hz. **d** Frequency response of VHB4910, Sylgard 184 and LA-CP-3 under 9 MV m^{-1} in the range of 1 Hz–500 Hz. **e** Variation of *z*-axis displacement during cyclic actuation test of 50,000 cycles. The enlarged image on the right shows the 30,000-30,010th cycles.

elastomer, possesses a gratifying frequency response performance comparable to silicones.

Furthermore, the LA-CP-3 demonstrates steady cyclic actuation response over 50,000 cycles, indicating excellent fatigue resistance and promising potential for practical applications (Fig. 3e).

Power density performance and high-speed DEA rotary motor

LA-CP-3 features both large area strains (indicating high energy density) and elevated response bandwidth (Fig. 3b, d), which exhibits the potential for high power density. The schematic diagram of dielectric elastomers testing configuration for power density and its equivalent

circuit model is demonstrated in Supplementary Fig. 11a. The measurement and calculation of the equivalent circuit parameters is described in "Measurement and discussion of equivalent circuit parameters" in the Supplementary Discussion and Supplementary Fig. 11. Owing to suppressed viscoelasticity and broad bandwidth, the electrically-driving area strain of LA-CP-3 fluctuates in low amplitude in the range of 10 ~ 100 Hz and exhibits a resonance peak at 200 Hz, followed by a sudden decline. At the resonance frequency of 200 Hz, LA-CP-3 achieves an area strain of 9.1% @20 MV m^{-1}, 3.5 times higher than that at 10 Hz (Fig. 4a). Assuming that dielectric elastomers are constant volume under small strain, the detailed derivation of energy density and power density from area strain and electric field is illustrated in "Calculation of power density under different driving frequencies" and "Calculation of area strain and true electric field" in the Supplementary Discussion and Supplementary Fig. 12. The variation of energy density with driving frequency is almost consistent with that of area strain, and the maximum energy density at resonance frequency is 744 J m^{-3} @20 MV m^{-1}, 200 Hz (Supplementary Fig. 13). Power density is the product of energy density and driving frequency. LA-CP-3 presents an impressive specific power density of 154 W kg^{-1}@ 20 MV m^{-1}, 200 Hz, about 75 times higher than that at 10 Hz (Fig. 4b). This performance rivals the power density range of natural human muscles, with a typical value of 50 W kg^{-1} and a maximum value reaching up to 284 W kg^{-1} [26]. A comparison of power density vs electric field with previously reported materials is illustrated in Fig. 4c while that of power density vs driving frequency in Fig.4d.

Besides the inherent features of dielectric elastomers like dielectric constant and Young's modulus, specific power density is closely related to driving electric field amplitude (usually call "electric field") and frequency. Specifically, it is proportional to the product of the fourth power of the electric field and frequency. Hence, improving driving electric field can effectively enhance the power density. However, high electric fields usually bring about the risk of electric shock and increase in cost and bulk of devices. Increasing electrically-driving area strain and driving frequency is a promising way to achieve high power density at low electric field. A common strategy to increase the area strain of elastomers is to elevate the dielectric constant and reduce Young's modulus, which usually results in severe viscoelasticity, thereby decreasing driving frequency. Incorporating high dielectric constant and high frequency together is of great challenge but the key to realizing high power density under low electrically-driving fields. LA-CP-3 combines the high dielectric constant of polyacrylates and the high response frequency of silicones, exhibiting high power density at a low electric field and high frequency (154 W kg^{-1} @20 MV m^{-1}, 200 Hz).

Rotary motors are essential in various applications, from robotics to home appliances. However, traditional electromagnetic motors, relying on heavy metallic components like copper windings and iron cores, are usually heavy and lack flexibility. This restricts their use in advanced, lightweight, and adaptable systems such as interactive actuators and soft robotics. Recent research has shown that dielectric elastomer actuators not only can produce rotary motion but also offer the benefits of flexibility, ease of control, and high specific energy/power density[15–18,39]. Herein, to further illustrate the significance of high power density of LA-CP-3, we have constructed a DEA rotary motor and measured its rotating speed under varied driving electric fields and frequencies.

The foundational operating principle of the DEA rotary motor, initially introduced by Anderson et al.[15] and depicted in Fig. 4e, involves a straightforward configuration comprising a DE film with compliant electrodes, an orbit gear, and a rotor gear. The DE film is segmented into four distinct sectors with electrodes. The orbit gear is anchored at the film's center, while the rotor gear is centered within the DEA assembly. In the unactuated state, the DE film, orbit gear, and rotor gear are concentrically aligned. Upon electrical actuating one sector, the film's center and the attached orbit gear translate towards the opposing sector, meshing with the rotor gear. Subsequently, by sequentially and cyclically actuating all four sectors with a phase difference of 90°, the orbit gear undergoes a two-dimensional translation, which is then converted into the rotational motion of the rotor gear.

The configuration and experimental setup of DEA rotary motor are illustrated in Methods and "Configuration and transmission of the DEA rotary motor" in the Supplementary Discussion and Supplementary Figs. 14–16. Prior to assessing the rotational speed characteristics of the motor, the voltage and current of a single section over time when subjected to a step voltage (1 kV) were recorded, as shown in Supplementary Fig. 17. The charging time is approximately 0.2 ms, significantly shorter than the electrically-driving time across the entire frequency range ($1/f_{max}*\alpha$, f_{max} is the highest driving frequency and α is the duty ratio of the square wave). Therefore, the effect of charging process on the rotating speed of the DEA motor is negligible and the rotating speed of DEA motor depends on electromechanical response of dielectric elastomer film.

Based on the transmission design, the target rotating speed can be theoretically calculated[39] ("Configuration and transmission of the DEA rotary motor" in the Supplementary Discussion). When the transmission gears mesh fully, the motor can match the target speed under relatively high voltage and certain frequencies. However, if the gears could not mesh as intended, primarily due to insufficient DE electrically-actuated strain, the output speed will be reduced. As the tooth number difference between the orbit gear and the rotor gear is three, the 2/3 target speed output might be attributed to the periodic inadequate meshing of skipping one tooth out of three per cycle while the 1/3 target speed output indicates skipping two teeth out of three per cycle. These incompletely meshing states suggest that the DE film works at insufficient actuation state, resulting in inadequate power.

Figure 4f illustrates the correlation between the rotational speed of the DEA motor and the frequency under electric field strengths of 16.8 MV/m, 17.9 MV/m, and 19.6 MV/m (Supplementary Movies 1–3). In the low-frequency range (<80 Hz), rotating speed rises linearly with the increase of driving frequency while almost independent on the driving electric fields. However, most of the rotating speeds only reach 1/3 target speed probably due to low actuation strain. Around 90 Hz, the rotating speed plunges because the actuation strain may decline to a threshold where the translation of orbit gear is much less that the transmission clearance between orbit gear and rotor gear, resulting in ineffective meshing between them. In this case, improving driving electric fields can apparently enhance the rotating speed.

Upon further increment of the frequency, the rotating speed surges remarkably and achieves its peak values within the bandwidth of 125 to 130 Hz across diverse electric fields. This indicates that the DE film reaches its highest power output at these frequencies, which are, in fact, the resonant frequencies. Notably, enhancing the driving electric field can elevate the peak speed effectively. At an electric field strength of 19.6 MV m^{-1} and frequencies ranging from 120 to 125 Hz, the motor realizes its theoretical target speed, signifying optimal meshing of the transmission gears. Moreover, the motor achieves maximum speed output of 1245 rpm at 19.6 MV m^{-1} and 125 Hz (Supplementary Movie 3). Figure 4g shows video captures of the motor rotating at 1245 rpm and the shaft rotates a full revolution in 48.2 ms. To the best of our knowledge, this performance places our DEA rotary motor in the exclusive high-speed domain of silicone-based motors, surpassing all previously reported DEA rotary motors based on acrylic elastomers, which typically operate at speeds less than 200 rpm, and rivals the speed of commercial electromagnetic two-phase micro stepper motors. Notably, the driving electric field of only 19.6 MV m^{-1} is significantly lower than that required by previously-reported DEA rotary motors (greater than 40 MV m^{-1}). Supplementary Table 1 summarizes the rotating speed characteristics of reported DEA rotary

https://doi.org/10.1038/s41467-024-54278-y

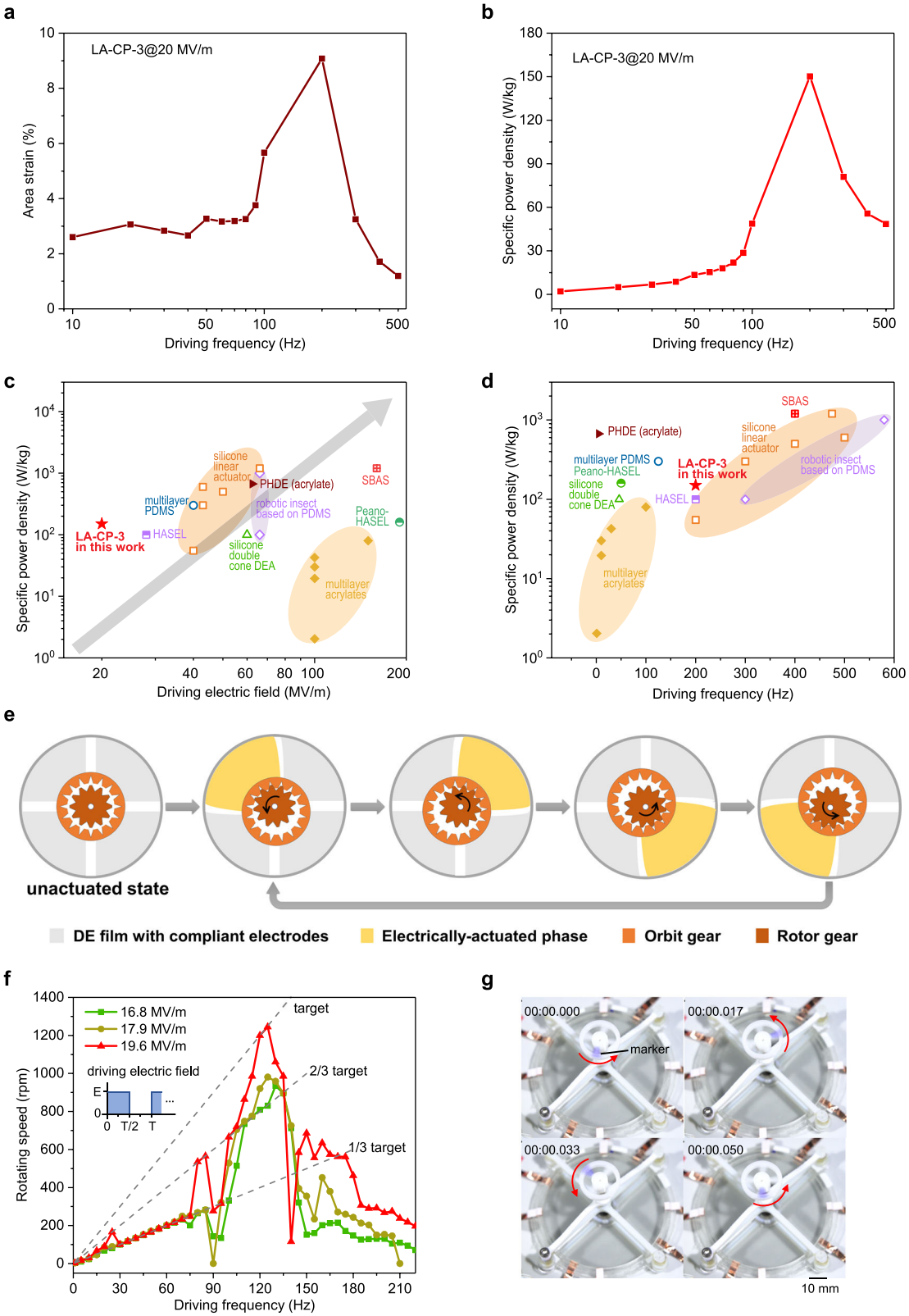

Fig. 4 | Power density characterization and high-speed DEA rotary motor under low electric fields. a Frequency dependence of actuated area strain for LA-CP-3 at 20 MV m^{-1}. **b** The relationship of specific power density calculated from area strain and electrically-driving frequency. The dimension of W m^{-3} and W kg^{-1} can be converted mutually via the density of LA-CP-3 (ρ = 970 kg m^{-3}). **c** Comparison of specific power density to driving electric field among LA-CP-3 (in this work), HASEL[41], multilayer PDMS[40], silicone double cone DEA[42], silicone linear actuator[4,11,22], PHDE (acrylates)[3], robotic insect based on PDMS[29], Peano-HASEL[43], multilayer acrylates[23,24]. **d** Comparison of specific power density to driving frequency among above materials. **e** The driving principle of the DEA rotary motor. **f** The rotating speed of DEA motor with driving frequencies under varied driving electric fields. The target rotating speed is theoretically calculated based on the transmission design. **g** Video captures of the DEA rotary motor at 1245 rpm. The scale bar is 10 mm.

motors. Over the resonant frequency, the speed of motor rapidly declines and shows another lower peak around 165 Hz. At high frequencies, the rotating speed is well below the theoretical value, probably owing to the severely deteriorated actuated strain. It is important to note that the frequency characteristics of DEA are not only dependent on the dielectric elastomer materials but also related to the configuration, electrode materials, driving schemes, and so on.

In a word, thanks to the high power density of LA-CP-3 at low electric fields and high driving frequencies, the DEA rotary motor in our work achieves the highest rotating speed (1245 rpm) among the state-of-the-art acrylate-based motors (<200 rpm), even under significantly reduced electric fields.

A bimodal network in polyacrylate elastomer has been crosslinked by two crosslinking agents with different molecular chain lengths to surmount several intrinsic shortages, demonstrating unusual electrically actuating response characteristics. This bimodal network demonstrates suppressed viscoelasticity due to moderately shortened average molecular length between crosslinking points and constrained molecular chain mobility, giving rise to reduced mechanical loss and elevated response frequency. In conclusion, the well-designed acrylate dielectric elastomer features the low mechanical loss and high response frequency (~200 Hz) like silicone elastomers, then realizing ultrahigh power density under a low electric field (154 W kg^{-1} @20 MV m^{-1}, 200 Hz) that reaches nature muscles. Further, a DEA rotary motor based on LA-CP-3 has been fabricated and realized maximum rotating speed of 1245 rpm under a greatly suppressed electric field (19.6 MV m^{-1} and 125 Hz), considerably higher than that of previously-reported acrylate-based motors and reaching the leading range of silicone-based motors. This work not only demonstrates an effective and general strategy for the fabrication of dielectric elastomers with high power density and broad response frequency bandwidth but also propels the applications of dielectric elastomers in low electric fields.

Methods

Materials

Lauryl acrylate (LA) used as the reactive monomer was purchased from Tokyo Chemical Industry Co., Ltd. CN9021NS from Sartomer Company was used as the macromolecular crosslinking agent and poly(ethylene glycol) diacrylate (PEGDA) from Shanghai Aladdin Biochemical Technology Co,. Ltd was used as the small-molecular crosslinking agent. The average molecular weight of CN9021NS and PEGDA is 2.8×10^4 g mol^{-1} [17] and ~516 g mol^{-1}, respectively. 2-Hydroxy-2-methyl propiophenone (HMPP) used as the photo-initiator was obtained from Shanghai Macklin Biochemical Co., Ltd. All the chemicals were used as received. A given mass of the above chemicals was mixed thoroughly by a vortex oscillator to form a homogeneous precursor solution. Supplementary Table 2 presents the specific formulations.

Preparation

The dielectric elastomers were synthesized by a UV curing method. A custom-made vessel comprising a silicone spacer sandwiched by release films and glass plates was fabricated to create an oxygen-free condition and tune the elastomer film thickness by adjusting the thickness of the silicone spacer. Release films were transparent polyethylene terephthalate (PET) films coated with silicone oil on the surface which help demolding. The precursor solution was injected into the designated vessel. Following this, it underwent curing in a UV curing reaction chamber, where it was exposed to a UV intensity of 2.5 W cm^{-2} for a duration of 3 min. This curing process was preceded by a vacuum degassing step that lasted 15 min. Once demolding was complete, the elastomer was transferred to a vacuum oven set at 40 °C for a period of 24 h to ensure the removal of any residual monomer. The nomenclature of samples was based on the composition and dose of chemicals, where LA stood for reactive monomer (LA), C for the macromolecular crosslinking agent (CN9021NS) while P for the small-molecular crosslinking agent (PEGDA), and these figures for the content of PEGDA. The PEGDA content of LA-CP-1, LA-CP-2, and LA-CP-3 is 0.2 wt%, 0.4 wt%, and 0.6 wt%, respectively.

Composition and thermal characterization

Gel experiment was conducted to analyze the network crosslinking density. Samples of 1 mm in thickness were cut into 10 mm × 10 mm squares and their initial mass was recorded. Following immersion in tetrahydrofuran (40 ml) for a week, the samples' dimensions were measured to calculate the swelling ratio (Q). This ratio is defined as the cube of the length of the elastomer after swelling divided by its original length. After drying the samples in a vacuum oven at 40 °C for 24 h, the final mass was determined to calculate the gel fraction. The gel fraction represents the ratio of the elastomer's mass before and after the swelling process. Differential scanning calorimetry (DSC) measurements were performed using a TA DSC250 machine at a ramping rate of 10 °C min^{-1} in a N_2 atmosphere. X-ray diffraction (XRD) characterization was carried out using glancing incidence on a Rigaku S2. Wide angle X-ray scattering (WAXS) analysis and small angle X-ray scattering (SAXS) analysis using SaxsLab GANESHA were conducted at 50 kV and 0.6 mA and the wavelength of X-ray is 0.154 nm (Cu target). XRD, WAXS and SAXS were performed at 20 °C.

Dielectric characterization

Dielectric properties in the range of 10^{-1} Hz to 10^7 Hz and 1 V (Vrms) were tested by a Broadband Dielectric Spectroscopy (Novocontrol Technologies GmbH&Co. KG) on circular specimens (diameter: 20 mm, thickness: 1 mm).

Mechanical characterization

Uniaxial stretch test using Instron 3343 was performed at the tensile rate of 200 mm min^{-1} until fracture to obtain stress vs tensile ratio curves and Young's moduli were defined as the slopes of tangent lines at 5% strain. Samples were cut into a dumbbell shape with an effective area of 2 mm width by 12 mm length and a thickness of 1 mm. Cyclic uniaxial tensile experiments were tested on a narrow strip of 10 mm (width) × 50 mm (length) × mm (thickness) (the gauge length was 30 mm) at the rate of 100 mm min^{-1}. Dynamic mechanical analysis (DMA) at 5% strain using a TA Q800 instrument under shear mode was performed at 25 °C and 0.1 Hz-100 Hz. The dimensions of the specimens were 10 mm × 10 mm × 1 mm.

Electrical strength characterization

The electrical strength of elastomers was tested using a high voltage tester (BDJC-50kV, Beijing, Beiguang) with 25-mm-diameter pillar-to-plate electrodes in silicone oil. A DC voltage of a ramping rate of 500 V s^{-1} was applied to 0.6-mm-thickness elastomers until the voltage drops sharply. The characteristic breakdown strength that corresponds to ~63.2% probability of failure was calculated from a linear fitting using two-parameter Weibull distribution across 10 specimens.

Preparation of the actuators and electrical actuation measurement

The nominal electric field was defined as the ratio of the applied voltage to the initial thickness of elastomer film before electrically-actuated deformation. 1-mm-thickness elastomer films were fixed on an annular PMMA rigid frame with an inner diameter of 20 mm (d = 20 mm) and coated by single-walled carbon nanotube electrodes (Nanjing XFNANO Materials Tech Co., Ltd) as compliant electrodes. And the carbon nanotube electrodes were prepared according to the literature[40]. The driving voltage was increased at a step of 1 kV until electric breakdown failure or 15 kV. A laser sensor (LK-g80, Keyence) was used to measure the sinkage depth (h) of the film center. The area

strain (s) was calculated by the equation: $s = (2h/d)^2 * 100\%$. For fatigue testing, a two-channel function generator (Tektronix, AFG31000) and a high voltage amplifier (Trek 30/20 A) combined to output square waveform driving electric field of 9 MV m^{-1}, 5 Hz, and 50% duty cycle. For frequency response characterization, the driving electric field was a sinusoidal wave whose amplitude was fixed to 9 MV m^{-1} and frequency was reduced from 500 Hz to 1 Hz. For power density measurement, the thickness of elastomer films was 0.3 mm, and the driving electric field was a sinusoidal wave with an amplitude of 20 MV m^{-1} and driving frequency was decreased from 500 Hz to 10 Hz. "Measurement and discussion of equivalent circuit parameters" in the Supplementary Discussion demonstrates the measurement and calculation of circuit parameters. And "Calculation of power density under different driving frequencies" and "Calculation of area strain and true electric field" in the Supplementary Discussion describe the calculation of area strains at different frequencies and the detailed derivation of energy density and power density from obtained area strains and driving electric fields.

Fabrication of the DEA rotary motor

The original thickness of DE film before pre-strain was 0.3 mm. Ultrapure single-walled carbon nanotubes (SWCNTs) aqueous dispersion (0.15% weight concentration, from Nanjing XFNANO Materials Tech Co., Ltd) was diluted by deionized water by a factor of 100, and 6 mL of this diluted solution was used to cast an electrode film onto a polyethersulfone membrane filter (90 mm disk diameter, 0.22 μm pore diameter, from Nantong Longjin Membrane Technology Co., Ltd) via vacuum filtration. The SWCNT electrodes were then transferred to DE films to create circular sectored electrodes with four sections using a precut 100-μm-thickness PET film mask. The DE film with patterned electrodes was pre-strained from a diameter of 54 mm to a diameter of 70 mm, and sandwiched by two rigid frames (inner diameter of 66 mm), which were connected to copper conductive tape leads (Supplementary Fig. 14). Before the subsequent assembly, we verified the actuation performance of DE film using a Digital Oscilloscope EDUX1002G (Keysight Technologies) to generate the low-voltage square waveforms of 1 Hz and a 615-3 High-Voltage AC/DC Generator (Trek Inc.) to amplify the signals by 1000 times. Each section was tested with high voltages of amplitudes ranging from 2 kV to 3.5 kV. Finally, the gears, DE film, braces, shaft, bearings, and wheel were assembled and secured with screws as depicted in Supplementary Fig. 15. The orbit and rotor gears (module is 0.3; tooth numbers are 21 and 18; transmission ratio is 6; meshed gears center distance is 0.541 mm; gear addendum radius difference is 0.210 mm) were fabricated via smart composite microstructure technology for precise manufacturing and weight reduction. For further details, please refer to the previous publication[39].

Experimental set and speed characterization of the DEA rotary motor

The diagram of driving and testing setup is shown in Supplementary Fig. 16. We utilized LabVIEW to produce the four-channel bipolar square wave signals with a 90° phase difference, which were then fed into four Trek 2220 high-voltage amplifiers via a NI USB-6363. To enhance the strength of the driving voltage, an additional high-voltage amplifier (Trek 615-3 with a Keysight EDUX1002G as control module) was adopted to generate a DC high voltage equivalent to the negative amplitude of the aforementioned square high voltage. Then, the reference terminals (namely ground terminals) of four Trek 2220 amplifiers were connected to that of Trek 615-3 amplifier to generate four-channel positive polarity square waves for electrically actuating four phases of DEA motor. A Sony Alpha 7 R III camera was employed to capture the motor's rotational movement with at a frame rate of 120 frames per minute (fpm).

Data availability

The authors declare that all data supporting the findings of this study are available within the article and the supplementary materials. Further information is available from the corresponding author upon request (dangzm@tsinghua.edu.cn).

References

1. Brochu, P. & Pei, Q. Advances in dielectric elastomers for actuators and artificial muscles. *Macromol. Rapid Commun.* **31**, 10 (2010).
2. Pelrine, R., Kornbluh, R., Pei, Q. B. & Joseph, J. High-speed electrically actuated elastomers with strain greater than 100%. *Science* **287**, 836–839 (2000).
3. Shi, Y. et al. A processable, high-performance dielectric elastomer and multilayering process. *Science* **377**, 228–232 (2022).
4. Chen, Y. et al. Controlled flight of a microrobot powered by soft artificial muscles. *Nature* **575**, 324–329 (2019).
5. Lu, T. Q., Ma, C. & Wang, T. J. Mechanics of dielectric elastomer structures: a review. *Extrem. Mech. Lett.* **38**, 100752 (2020).
6. Ning, N. et al. Tailoring dielectric and actuated properties of elastomer composites by bioinspired poly(dopamine) encapsulated graphene oxide. *ACS Appl. Mater. Interfaces* **7**, 10755 (2015).
7. Tang, C. et al. A review on high-frequency dielectric elastomer actuators: materials, dynamics, and applications. *Adv. Intell. Syst.* **6**, 2300047 (2023).
8. Shintake, J., Cacucciolo, V., Shea, H. & Floreano, D. Soft biomimetic fish robot made of dielectric elastomer actuators. *Soft Robot* **5**, 466 (2018).
9. Ji, X. et al. Untethered feel-through haptics using 18-μm thick dielectric elastomer actuators. *Adv. Funct. Mater.* **31**, 2006639 (2020).
10. Poulin, A., Demir, C. S., Rosset, S. T., Petrova, V. & Shea, H. Dielectric elastomer actuator for mechanical loading of 2D cell cultures. *Lab Chip* **16**, 3788 (2016).
11. Chen, Y. F., Xu, S. Y., Ren, Z. J. & Chirarattananon, P. Collision resilient insect-scale soft-actuated aerial robots with high agility. *IEEE Trans. Robot.* **37**, 1752 (2021).
12. Ren, Z. et al. A high-lift micro-aerial-robot powered by low-voltage and long-endurance dielectric elastomer actuators. *Adv. Mater.* **34**, 2106757 (2022).
13. Gu, G., Zou, J., Zhao, R., Zhao, X. & Zhu, X. Soft wall-climbing robots. *Sci. Robot.* **3**, eaat2874 (2018).
14. Li, G. et al. Self-powered soft robot in the Mariana Trench. *Nature* **591**, 66 (2021).
15. Anderson, I. A. et al. A dielectric elastomer actuator thin membrane rotary motor. *Proc. SPIE-Int. Soc. Opt. Eng.* **7287**, 72871H (2009).
16. Anderson, I. A. et al. A thin membrane artificial muscle rotary motor. *Appl. Phys. A: Mater. Sci. Process.* **98**, 75 (2010).
17. Yin, L. J. et al. Soft, tough, and fast polyacrylate dielectric elastomer for non-magnetic motor. *Nat. Commun.* **12**, 4517 (2021).
18. Rosset, S. & Shea, H. Towards fast, reliable, and manufacturable DEAs: miniaturized motor and Rupert the rolling robot. *Proc. SPIE EAPAD* **9430**, 943009 (2015).
19. Shian, S., Bertoldi, K. & Clarke, D. R. Dielectric elastomer based "grippers" for soft robotics. *Adv. Mater.* **27**, 6814 (2015).
20. Shintake, J., Cacucciolo, V., Floreano, D. & Shea, H. Soft robotic grippers. *Adv. Mater.* **30**, 1707035 (2018).
21. Maffli, L., Rosset, S., Ghilardi, M., Carpi, F. & Shea, H. Ultrafast all-polymer electrically tunable silicone lenses. *Adv. Funct. Mater.* **25**, 1656 (2015).
22. Zhao, H. et al. Compact dielectric elastomer linear actuators. *Adv. Funct. Mater.* **28**, 1804328 (2018).
23. Mirvakili, S. M. & Hunter, I. W. Artificial muscles: mechanisms, applications, and challenges. *Adv. Mater.* **30**, 1704407 (2018).

24. Duduta, M., Hajiesmaili, E., Zhao, H., Wood, R. J. & Clarke, D. R. Realizing the potential of dielectric elastomer artificial muscles. *Proc. Natl Acad. Sci. USA.* **116**, 2476 (2019).
25. Duduta, M., Wood, R. J. & Clarke, D. R. Multilayer dielectric elastomers for fast, programmable actuation without prestretch. *Adv. Mater.* **28**, 8058 (2016).
26. Kornbluh, R., Pelrine, R., Pei, Q. B., Oh, S. & Joseph, J. Ultrahigh strain response of field-actuated elastomeric polymers. *Proc. SPIE EAPAD* **3987**, 51 (2000).
27. Kofod, G., Sommer-Larsen, P., Kronbluh, R. & Pelrine, R. Actuation response of polyacrylate dielectric elastomers. *J. Intell. Mater. Syst. Struct.* **14**, 787 (2003).
28. Han, Z. Q. et al. Hybrid fabrication of prestrain-locked acrylic dielectric elastomer thin films and multilayer stacks. *Macromol. Rapid Commun.* **44**, 2300160 (2023).
29. Ji, X. et al. An autonomous untethered fast soft robotic insect driven by low-voltage dielectric elastomer actuators. *Sci. Robot.* **4**, eaaz6451 (2019).
30. Hu, Y. F. & Majidi, C. Dielectric elastomers with liquid metal and polydopamine-coated graphene oxide inclusions. *ACS Appl. Mater. Interfaces* **15**, 24769 (2023).
31. Mao, J., Li, T. & Luo, Y. Significantly improved electromechanical performance of dielectric elastomers via alkyl side-chain engineering. *J. Mater. Chem. C.* **5**, 6834 (2017).
32. Ren, Z. et al. Phase-changing bistable electroactive polymer exhibiting sharp rigid-to-rubbery transition. *Macromolecules* **49**, 134 (2016).
33. Qiu, Y., Lu, Z. Y. & Pei, Q. B. Refreshable tactile display based on a bistable electroactive polymer and a stretchable serpentine joule heating electrode. *ACS Appl. Mater. Interfaces* **10**, 24807 (2018).
34. Gao, M., Meng, Y., Shen, C. & Pei, Q. Stiffness variable polymers comprising phase-changing side-chains: material syntheses and application explorations. *Adv. Mater.* **34**, 2109798 (2022).
35. Feng, W. et al. A large-strain and ultrahigh energy density dielectric elastomer for fast moving soft robot. *Nat. Commun.* **15**, 4222 (2024).
36. Suo, Z. Theory of dielectric elastomers. *Acta Mech. Solid. Sin.* **23**, 549 (2010).
37. Zhao, X. & Suo, Z. Theory of dielectric elastomers capable of giant deformation of actuation. *Phys. Rev. Lett.* **104**, 178302 (2010).
38. Niu, X. et al. Synthesizing a new dielectric elastomer exhibiting large actuation strain and suppressed electromechanical instability without prestretching. *J. Polym. Sci., Part B: Polym. Phys.* **51**, 197 (2013).
39. Du, B. et al. High-speed rotary motor for multidomain operations driven by resonant dielectric elastomer actuators. *Adv. Intell. Syst.* **5**, 2300243 (2023).
40. Jiang, S. W., Tang, C., Liu, X. J. & Zhao, H. C. Long-life-cycle and damage-recovery artificial muscles via controllable and observable self-clearing process. *Adv. Eng. Mater.* **24**, 2101017 (2021).
41. Leroy, E., Hinchet, R. & Shea, H. Multimode hydraulically amplified electrostatic actuators for wearable haptics. *Adv. Mater.* **32**, 2002564 (2020).
42. Cao, C. L., Burgess, S. & Conn, A. T. Toward a dielectric elastomer resonator driven flapping wing micro air vehicle. *Front. Robot. AI* **5**, 137 (2019).
43. Kellaris, N., Venkata, V. G., Smith, G. M., Mitchell, S. K. & Keplinger, C. Peano-HASEL actuators: muscle-mimetic, electrohydraulic transducers that linearly contract on activation. *Sci. Robot.* **3**, eaar3276 (2018).

Acknowledgements

This work was financially supported by National Natural Science Foundation of China (Nos. 52437002, 52307024, 51937007 and 52377031), China Postdoctoral Science Foundation (Nos. 2022TQ0167 and 2022M721777) and State Key Laboratory of Electrical Insulation and Power Equipment (EIPE23209).

Author contributions

Z.M.D. and L.J.Y. conceived the idea. L.J.Y., Z.M.D., B.D., and Y.Z. designed the experiments. L.J.Y., H.Y.H., W.Z.D. and Y.Z. carried out the experiments. L.J.Y. and H.Y.H. carried out the electrical actuation testing. L.J.Y. and B.D. fabricated DEA rotary motor and carried out related experiments. L.J.Y., Z.M.D., H.Z., Y.Z., Z.Z., C.Y., S.L.Z., and L.Q. analyzed the data. L.J.Y., Z.M.D., and Y.Z. wrote the manuscript. All authors discussed the results and commented on the manuscript.

Competing interests

The authors declare no competing interests.

Additional information

Supplementary information The online version contains Supplementary Material available at https://doi.org/10.1038/s41467-024-54278-y.

Correspondence and requests for materials should be addressed to Zhi-Min Dang.

Peer review information *Nature Communications* thanks Xiaozhen Du, Mihai Duduta and Yunhua Zhao for their contribution to the peer review of this work. A peer review file is available.